

# Solvent-free mechanochemical synthesis of ultrasmall nickel phosphide nanoparticles and their application as a catalyst for the hydrogen evolution reaction (HER)

Blaine G. Fiss<sup>1</sup>, Nhu Nang Vu<sup>2</sup>, Georgia Douglas<sup>1</sup>, Trong-On Do<sup>2\*</sup>, Tomislav Friščić<sup>1\*</sup>, Audrey Moores<sup>1,3\*</sup>

1. Centre in Green Chemistry and Catalysis, Department of Chemistry, McGill University, 801 Sherbrooke Street West, Montréal, Québec H3A 0B8, Canada

2. Department of Chemical Engineering, Laval University, Québec City, Québec G1V 0A6, Canada

3. Department of Materials Engineering, McGill University, 3610 University Street, Montréal, Québec H3A 0C5, Canada

**KEYWORDS:** Mechanochemistry, nickel phosphide, graphitic carbon nitride, hydrogen evolution, photocatalysis

\*E-mail: audrey.moores@mcgill.ca

\*E-mail: tomislav.friscic@mcgill.ca

\*E-mail: trong-on.do@gch.ulaval.ca

*Dedicated to Dr. Terrence "Terry" Fiss who sadly passed away after a long battle with cancer during the preparation of this manuscript. Uncle Terry had always been one of my strongest supporters in my pursuit towards a career in science, always encouraging me to tackle tough problems, and never stop asking questions.*

---

**ABSTRACT:** The photocatalytic (PC) splitting of water into oxygen and hydrogen has attracted considerable attention in the last decade. Despite the promise of hydrogen gas as a new energy resource, the environmentally-friendly design of viable catalysts with good morphological and size control remains a continual challenge. Of the many classes of available catalysts, metal phosphides are a low-cost and potentially accessible option as catalysts for this reaction, compared to the traditionally used precious metal catalysts. However, the synthesis of metal phosphide nanomaterials currently involves the use of highly reactive phosphorus sources at high temperatures in organic solvents. Herein, we demonstrate the application of sodium phosphide as an excellent solid-state phosphorus source for the synthesis of nickel phosphide nanoparticles below 3 nm in diameter, a size range previously unheard of for mechanochemical synthesis of metal phosphides. These nanoparticles in turn showed success for the hydrogen evolution reaction, using graphitic carbon nitride as a photocatalytic support, generating 233.9  $\mu\text{mol g}^{-1} \text{h}^{-1}$  of hydrogen, using broad spectrum light at room temperature after only 3 hours, as well as being readily recyclable and reusable, without any decrease in reactivity. This mechanochemical method shows a mass intensity (MI) value over 2.5 times lower than traditionally used solution-based methods, even after workup and washing of the product. Upon scaling up the reaction to a 2.5 gram scale, we were able to further improve the MI to 3 times lower than traditional solvent based methods, while reducing the energy demand over 18-fold.

---

The research and use of metal-based quantum dots has shown great potential in applications ranging from medical imaging,<sup>1,2</sup> as optical materials<sup>3</sup> and catalysts, including water-splitting,<sup>4</sup> for the production of hydrogen as an alternative fuel source.<sup>5</sup> Various environmentally and energy conscious methods have been employed to produce single atom or transition metal sulfide<sup>6</sup> catalysts to reduce overall cost compared to the traditionally employed supported platinum catalysts. In particular, transition metal phosphide nanoparticles (TMP NPs)

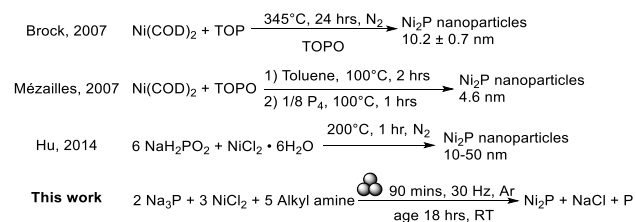
have attracted attention as recoverable, cost effective catalysts for hydrogen evolution reaction (HER),<sup>7-10</sup> hydrodesulfurization,<sup>11-13</sup> hydrodenitrogenation,<sup>14,15</sup> hydrodeoxygenation<sup>16-19</sup> along with a recent example of photocatalytic C-C bond forming reactions.<sup>20</sup> Among these, the most promising have been metal phosphide nanoparticles based on earth-abundant metals such as iron, cobalt and nickel.<sup>9</sup> Two main synthetic approaches have been investigated for the synthesis of metal phosphide nanoparticles, specifically those based on nickel.

First are methods involving the thermal decomposition of pre-made transition metal phosphine or phosphite complexes,<sup>21</sup> affording well defined metal phosphide NPs, as shown by the Brock<sup>13</sup> or Hu<sup>10</sup> groups. Second, ready-made zero valent metal nanoparticles are reacted with zero-valent phosphorus sources, such as white phosphorus (P<sub>4</sub>), as seen in the work of Mézailles and coworkers (Scheme 1).<sup>22</sup> However, both types of approaches employ phosphorus-containing compounds that are either hazardous, such as P<sub>4</sub>,<sup>21,23</sup> or require a large amount of energy input to activate them, such as trioctylphosphine (TOP).<sup>7,21,23,24</sup> While red phosphorus can also be employed as a precursor, its use requires significantly longer runtimes (20-40 hours),<sup>25,26</sup> often in a large excess of solvent.

Mechanochemistry has been increasingly researched as an effective synthetic method to access a wide range of materials,<sup>27</sup> including polymers,<sup>28-31</sup> Perovskites<sup>32</sup> and metal organic frameworks (MOFs).<sup>33-35</sup> Mechanochemistry is associated with sustainability benefits such as the reduced use of bulk solvent and lower input energy, being listed by IUPAC as one of the Top 10 chemical innovations towards a sustainable future.<sup>36</sup> The application of mechanochemistry to the area of main-group and phosphorus chemistry has been gaining gradual traction.<sup>37</sup> This includes the synthesis of regiospecific phosphazanes,<sup>38</sup> or sterically encumbered phosphazanes whose synthesis was only achieved using ball-milling techniques.<sup>39</sup> This background work gave a strong precedent for the application of mechanochemistry towards the activation of a simple, metastable phosphide source, namely Na<sub>3</sub>P, which was both easy to synthesize and handle under air-free conditions and yet, could be activated at room temperature. Alkali phosphides like sodium phosphide have long been known, both their fundamental study in main-group structure and bonding, as well as solid forms of phosphine gas by hydrolysis.<sup>40</sup> Early solid-state metathesis work indicated that light grinding of early transition metal halides (TaCl<sub>5</sub>, NbCl<sub>5</sub> and MoCl<sub>5</sub>) with sodium phosphide can lead to the formation of transition metal phosphides, but in these cases, only the bulk material was observed.<sup>41</sup> This early work, as well as the mechanochemical synthesis of bulk metal phosphides using elemental precursors, in which metal powders are milled together with red phosphorus over longer timescales (3-40 hours),<sup>42-44</sup> are appealing approaches to access these important materials. Yet the control over the structure of such materials at the nanoscale is absolutely essential, in particular for applications towards catalysis in which high surface area for better reactivity is crucial or applications relying on tuneable optical properties.<sup>45</sup>

Mechanochemistry has been proven a powerful means to access heterogeneous catalysts through more benign pathways,<sup>46,47</sup> including nanoparticles (NPs) of precious metals<sup>48</sup> or binary metal sulfide quantum dots.<sup>49-53</sup> Mechanochemical methods of metal sulfide synthesis were shown to allow access to a variety of NP shapes, such as nanorods of copper sulfide<sup>54</sup> and has even been shown to be a viable synthetic method towards the semi-industrial synthesis of quaternary metal sulfides for photovoltaic applications.<sup>55</sup> It has also been used to make bioinspired nanoparticle composites for both oxidation and water-splitting, employing titania supported proteins<sup>56</sup> and pre-made silver nanoparticles on a carbon nitride support with hemoglobin proteins respectively.<sup>57</sup> Good size and shape control is often obtained through the use of a bottom-up method, in which the NP precursors are milled with a suitable ligand, typically containing long alkyl chains.<sup>58</sup>

Herein we describe a mechanochemical approach for the synthesis of ultrasmall nickel phosphide NPs using a novel bottom-up approach in the presence of long chain amines and their potential use as water-splitting cocatalysts paired with graphitic carbon nitride (g-C<sub>3</sub>N<sub>4</sub>).



Scheme 1. Select examples of nickel phosphide nanoparticle synthesis, both in solution, as well as mechanochemically

## Results and Discussion

### Effect of ligand chain-length and ligand loading

The herein presented synthesis of nickel phosphide nanoparticles is based on a general approach involving milling of anhydrous nickel chloride, sodium phosphide and a capping ligand. In a typical experiment, the reaction components were milled together in a zirconia milling jar with a 10 mm zirconia ball for 90 minutes at 30 Hz. The samples were then left sealed and allowed to age at room temperature for 18 hours prior to washing via centrifugation and drying *in vacuo*. Characterization was conducted using Transmission Electron Microscopy (TEM), Energy-Dispersive X-Ray (EDX) Spectroscopy, X-ray Photoelectron Spectroscopy (XPS) and Powder X-ray diffraction (PXRD) to evaluate the size, morphology and crystallinity of the nickel phosphide phases formed by milling. We tested two ligand parameters for their influence on the final size and stability of the produced particles: 1) the chain length of the alkyl amine ligands; 2) the binding strength of each ligand, by testing both traditionally used amines, as well as phosphines. The choice of amines was based on past successful experience in our group for the mechanochemical formation of Au and Bi<sub>2</sub>S<sub>3</sub> NPs.<sup>48,49</sup> In these examples, it was believed that the lability of the metal-amine bond, contributed to growth control. Initial exploration of a shorter (C15) pentadecylamine ligands confirmed the ability to obtain nanoparticle material, albeit with broad particle size distributions of 3.5 ± 1.2 and 4.8 ± 2.1 nm when using 2 and 5 molar equivalents in the reaction respectively (Table 1, Entries 1 and 2; Figures S6 and S7). Increasing the chain length from C15 to C16, by using 2 or 5 molar equivalents of hexadecylamine produced nanoparticles of 3.5 ± 0.8 nm and 5.4 ± 1.3 nm diameters, respectively (Table 1, Entries 3 and 4; Figures S8 and S9). The use of heptadecylamine, a C17-substituted amine, provided more consistent outcomes of the mechanochemical synthesis, giving particles with an average diameter of 5.0 ± 2.1 nm and 2.8 ± 0.6 nm for 2 and 5 molar equivalents respectively (Table 1, Entries 5 and 6; Figures S10 and Figure 1). Traditionally used liquid ligands such as oleylamine (Table 1, Entry 7; Figure S11) and trioctylphosphine (TOP) (Table 1, Entries 8 and 9; Figure S12 and S13) were also tested. Milling with oleylamine produced discrete yet aggregated particles, with average particle size of 3.0 ± 0.8 nm. When using TOP, a mixture of both small aggregated particles, as well as larger, more discrete particles were

seen, indicating slower rates of nucleation compared to heterogeneous nucleation and particle growth. The presence of Ni(0), was also detected by XPS (Figure S18b) suggesting TOP was reducing the NiCl<sub>2</sub> at a faster rate compared to phosphide formation, also supported by the smaller shoulder as shown in the phosphorus focused scan compared to the samples made with alkyl amine ligands, for which the signal is more distinct (Figure S18a). In all cases using alkylamine ligands, particles showed the presence of both Ni and P, at binding energies of 7.5 and 2 keV respectively, as proven through EDX analysis (Figure S17). Since the use of 5 molar equivalents of heptadecylamine consistently gave particles with diameters below 3 nm, offering more available surface area for catalytic activity, we focused on this amine as the standard ligand in all subsequent tests.

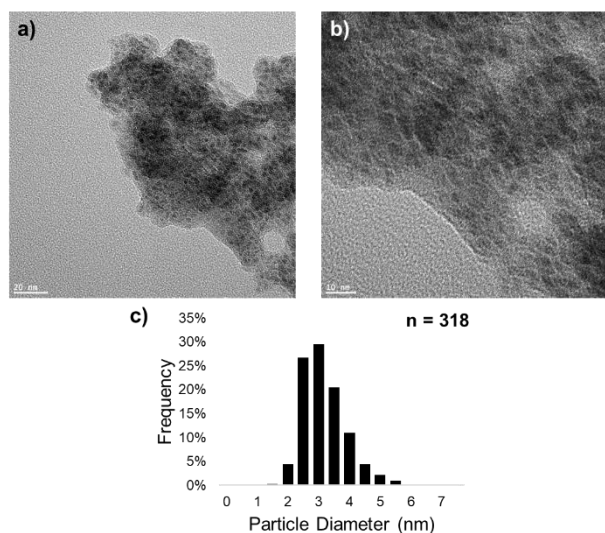


Figure 1. TEM images (a) and b)) and histogram of particle size distribution (c) of nickel phosphide nanoparticles made using 5 equivalents of heptadecylamine ligand, using a 3:2 ratio of NiCl<sub>2</sub> and Na<sub>3</sub>P (Ni<sub>x</sub>P<sub>y</sub>-5-C17)

Table 1. Effect of alkyl amine chain length as well as ligand equivalency on final metal phosphide particle sizes

Entry	Sample name	Ligand	Ligand equivalents	Particle size (nm)
1	Ni <sub>x</sub> P <sub>y</sub> -2-C15	Pentadecylamine	2	3.5 ± 1.2
2	Ni <sub>x</sub> P <sub>y</sub> -5-C15	Pentadecylamine	5	4.8 ± 2.1 <sup>a</sup>
3	Ni <sub>x</sub> P <sub>y</sub> -2-C16	Hexadecylamine	2	3.5 ± 0.8

4	Ni <sub>x</sub> P <sub>y</sub> -5-C16	Hexadecylamine	5	5.4 ± 1.3
5	Ni <sub>x</sub> P <sub>y</sub> -2-C17	Heptadecylamine	2	5.0 ± 2.1
6	Ni <sub>x</sub> P <sub>y</sub> -5-C17	Heptadecylamine	5	2.8 ± 0.6
7	Ni <sub>x</sub> P <sub>y</sub> -10-OAm	Oleylamine	10	3.0 ± 0.8
8	Ni <sub>x</sub> P <sub>y</sub> -2-TOP	TOP	2	Mix of small particle aggregates and larger particles
9	Ni <sub>x</sub> P <sub>y</sub> -5-TOP	TOP	5	Mix of small particle aggregates and larger particles

a: A mixture of free and aggregated particles were noted by bright field TEM microscopy

The surface composition of Ni<sub>x</sub>P<sub>y</sub>-5-C17 was validated through XPS analysis. The survey scans showed the presence of oxygen, nickel and phosphorus throughout the materials surface, which supports the formation of nickel phosphate, alongside residual sodium and chlorine peaks, stemming from sodium chloride by-product still on the surface (Figure S19). The XPS analysis indicated a nickel phosphide phase with Ni-P covalent bonds. Notably, the observed binding energy of Ni2p (852.88 eV, Figure 2a) is higher than that of Ni metal (852.6 eV) while the observed binding energy of P2p (129.98 eV, Figure 2b) is red-shifted compared to that of the elemental P (around 130eV), revealing a Ni<sup>δ+</sup>P<sup>δ-</sup> electronic state.<sup>59</sup> The nickel-focused scan also showed two additional signals at 856.28 and 873.88 eV, matching closely with previously reported peaks of Ni-O bonds, due to partial surface oxidation (Figure 2a).<sup>60</sup> This surface oxidation was also validated by the phosphorus-focused scan of the 2p orbital with a second maximum at 133.28 eV (Figure 2b).<sup>61</sup> Looking also to the oxygen 1s scan, two major peaks can be seen, the first at 531.38 eV has been well documented as the -OH signal for both hydroxyl and P-OH groups on the surface (Figure 2c).<sup>62,63</sup> The carbon focused 1s scan (Figure 2d) showed 3 distinct peaks, the first at 284.88 and 286.28 eV corresponding to the C-C and C-N bonds found in the surface capping alkyl amine ligands. The last peak at 288.88 eV is indicative of a C=O bond, most likely due to surface absorbed CO<sub>2</sub> for their storage under ambient conditions<sup>62</sup>

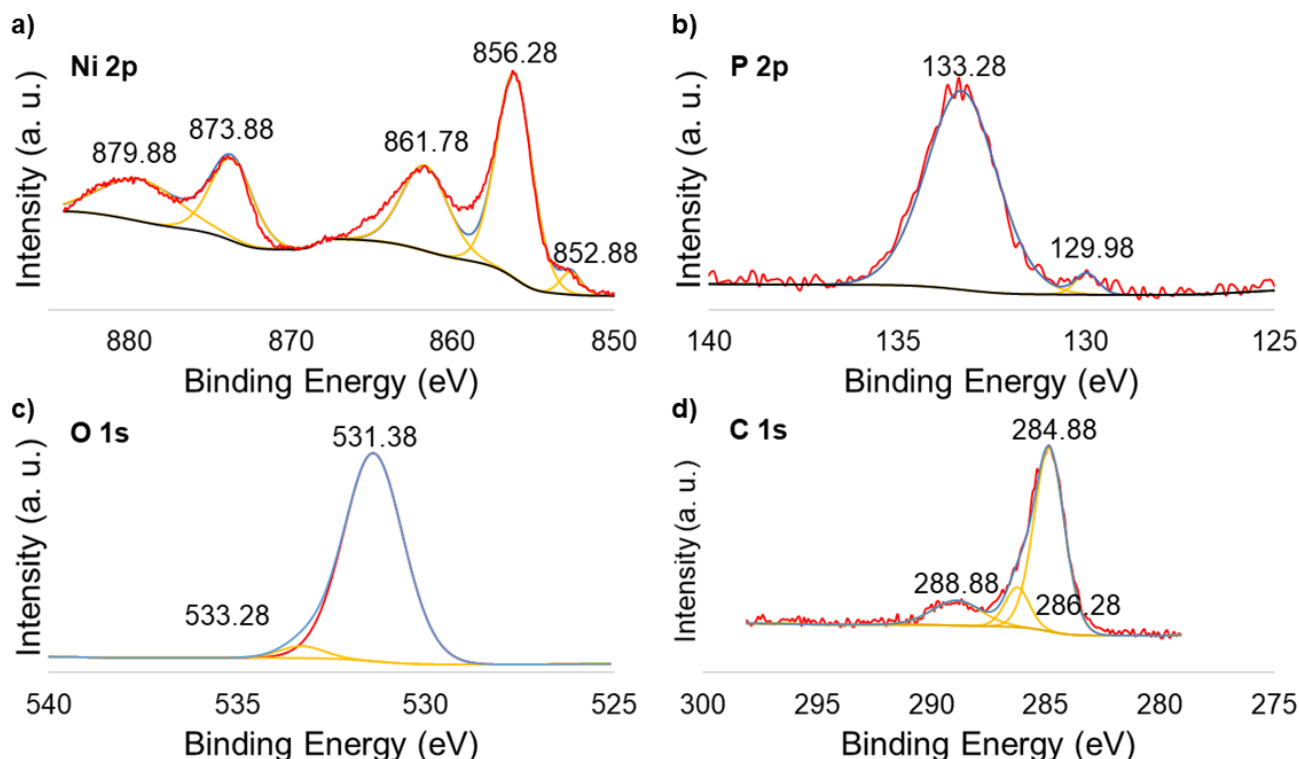


Figure 2. XPS focused scans of a) nickel 2p, b) phosphorus 2p, c) oxygen 1s and d) carbon 1s orbitals of freshly made nickel phosphide nanoparticles made using 3 equivalents of nickel chloride, 2 equivalents of sodium phosphide and 5 equivalents of heptadecylamine ligand ( $\text{Ni}_x\text{P}_y\text{-5-C17}$ )

The surface functionalization of the nickel phosphide nanoparticles made by milling was also confirmed using ATR-FTIR. Specifically, analysis of the dried powder catalyst revealed a pair of bands at  $2360\text{ cm}^{-1}$  and  $2340\text{ cm}^{-1}$  indicative of C-H stretches found in the surface alkyl amine ligands, as well as a large distinct signal at  $1057\text{ cm}^{-1}$ , indicative of the P=O double bond vibration due to partial oxidation<sup>64</sup> (Figure S24).

The organic/inorganic ratio in the mechanochemically synthesized nickel phosphide NPs was investigated using TGA (see ESI, Figure S26), revealing that 67% was composed of inorganic matter while the rest was constituted of the ligand shell, shown in three distinct regions. The first from 25 to  $225^\circ\text{C}$  can be attributed to the loss of surface water (13.5% loss), the second from  $225\text{-}375^\circ\text{C}$  which we hypothesize to be the thermal decomposition of the heptadecylamine ligand on the surface (8.5% loss), thus coating the surface in a thin carbon layer. The final loss beyond  $375^\circ\text{C}$  is the thermal decomposition of that subsequent carbon layer (10.9% loss).

#### Effect of varying the aging time on particle formation

Following our group's previous work on the mechanochemical synthesis of both gold and bismuth sulfide NPs,<sup>48,49</sup> it was noted that the impact and shear forces imposed by milling only worked to activate the precursors, while aging the samples allowed for the self-assembly of discrete NPs. We

set out to investigate this effect for the synthesis of ultrasmall nickel phosphide NPs by following the same milling procedure, this time only aging for 1, 3 or 6 hours.

Visual analysis of the samples following milling and aging showed black powders formed in all three cases, with no visual difference seen when varying the aging time. While further analysis by TEM showed the generation of some ultrasmall particles in each case, samples were largely made of bulk material, with the ultrasmall particles being a rarer exception (Figures S14-S16). This supports the hypothesis that aging under air-free conditions for 18 hours ensures the consistent formation of ultrasmall, monodisperse particles.

#### Phase control and crystal structure

Analysis of mechanochemically prepared samples by PXRD did not reveal any Bragg reflections matching  $\text{Ni}_2\text{P}$  patterns described in the literature (Figure S22).<sup>65</sup> The lack of crystallinity or X-ray reflections for a specific phase can be attributed to the minute size of particles overall, which can lead to significant broadening of diffraction signals, to the point where they become non-distinguishable from the background noise.<sup>49</sup>

Next, we explored how the stoichiometry of precursors would influence the final phase of NPs. Initially, our reactions focused on using a 3:2 molar ratio of  $\text{NiCl}_2$  to sodium phosphide, typically in the presence of 5 molar equivalents of our alkylamine capping ligand. However, other stoichiometric ratios were tested to investigate if specific, potentially more kinetically favoured phases of nickel phosphide NPs could be iso-

lated. This investigation began with the testing of Ni:P stoichiometric ratios of 2:1 and 5:4, in the attempt to make the thermodynamically favored Ni<sub>2</sub>P as well as the catalytically relevant Ni<sub>5</sub>P<sub>4</sub> phases.<sup>66</sup> Upon milling together anhydrous NiCl<sub>2</sub> and Na<sub>3</sub>P in a 2:1 stoichiometry, a black powder was produced. The PXRD pattern for these samples was featureless, indicating the formation of an amorphous product (Figure S23). Apart from the samples originally tested with a 3:2 stoichiometric ratio of Ni:P, we also investigated how changes to the initial ratio of nickel and phosphide sources would affect the reaction. However, all subsequently tested samples showed no distinct Bragg reflections for either Ni<sub>2</sub>P, Ni<sub>5</sub>P<sub>4</sub>, or NiP<sub>3</sub> phases, indicating that changes to the initial reaction stoichiometry lead to amorphous samples (Figure S23).

Information on the composition of the produced NPs was subsequently obtained *via* XPS, enabled by their diameters being below 3 nm. The survey scans of the nickel phosphide nanoparticles, both the small scale and gram scale mechanochemical syntheses, were used to determine the stoichiometries (see Table S1 in ESI for details). For the nickel phosphide made in the shaker mill, the determined stoichiometry was shown to be Ni<sub>2.3</sub>PO<sub>6.3</sub>. This supports our hypothesis that the formed cores have a Ni<sub>2</sub>P stoichiometry, with a partially oxidized phosphate surface, while excess oxygen is seen as a result of surface adsorbed CO<sub>2</sub> and H<sub>2</sub>O.

#### Multigram-scale synthesis of Ni<sub>x</sub>P<sub>y</sub>-5-C17

We were successful in scaling up our synthesis using a planetary mill, up to a 2.5 gram scale. XPS analysis of the scaled-up product also showed the presence of Ni, P, O and C as seen before as well as Na and Cl, similar to the small-scale survey scan (Figure S20). The focused P 2p showed peak energies at 128.88 eV and 132.68 eV closely matching the energies seen for the small-scale synthesis (Figure S21a). This story was also true for the Ni 2p focused scan, with key peak energies at 855.08 eV, 861.28 eV, 872.68 eV and 881.28 eV (Figure S21b), with a very good agreement with our small scale XPS data. The stoichiometry was determined to be Ni<sub>1.9</sub>PO<sub>8</sub>, based on XPS survey data. The series of results we obtained from XPS on the NP phase strongly suggest that we have a Ni<sub>2</sub>P core, covered with a thin shell of partially oxidized material. For simplicity, from now on, we will call Ni<sub>x</sub>P<sub>y</sub>-5-C17 samples Ni<sub>2</sub>P.

#### Deposition of mechanochemically synthesized Ni<sub>2</sub>P onto g-C<sub>3</sub>N<sub>4</sub> and characterization

An initial series of catalysts were synthesized through a direct mixing of Ni<sub>2</sub>P powder with g-C<sub>3</sub>N<sub>4</sub>, by combining 1 gram of bulk g-C<sub>3</sub>N<sub>4</sub>, with 0.03 grams of Ni<sub>2</sub>P powder in anhydrous ethanol for 30 minutes, followed by drying and annealing at either 300°C (samples CN-NiP-300) or 400°C (samples CN-NiP-400, see ESI Figures S1 for details). A second series of hybrid catalysts was made by first conducting a ligand exchange on the Ni<sub>2</sub>P cocatalyst to make them more water soluble. This was done by first sonicating 300 mg of Ni<sub>2</sub>P powder in a tetraethylammonium hydroxide solution (1 g in 1:1 ethanol : water mixture, v/v) for 30 minutes before stirring for 24 hours. The particles were then precipitated using 200 mL of acetone several times before resuspending in water (Figure S3). This suspension was then added to a solution of g-C<sub>3</sub>N<sub>4</sub>, which has been protonated with 1 M HCl, (see Figure S2) and stirred for 12 hours before annealing the final product at 400°C for 4 hours (Figure S4). Two varieties of composite catalyst were made using this method, the first, which was washed by centrifugation prior to annealing, with each annealing temperature listed at the end (for example, a sample centrifuged and then annealed at 300°C is denoted CN-NiP-Ex-300, see Figure S4 in ESI) with the second series being annealed directly after drying at 60°C, without any centrifugation (denoted CN-NiP-Im-300 if annealed at 300°C, see Figure S4 in ESI). Once the Ni<sub>2</sub>P nanoparticles had undergone ligand exchange and were mounted on the g-C<sub>3</sub>N<sub>4</sub> support, their morphology, surface chemistry and thermal stability were further investigated by TEM, XPS, ATR-FTIR and TGA. Analysis of the Ni<sub>2</sub>P onto g-C<sub>3</sub>N<sub>4</sub> composite photocatalyst by XPS revealed partial oxidation of the Ni<sub>2</sub>P NPs (Figure 3a, 3b and 3c), showing the presence of phosphorus in the form of surface phosphates as shown by the signal in the focused scan of the phosphorus 2p orbital at 133.38 eV (Figure 3b), similar to the as-made particles. The surface oxidation is likely due to exposure to air. The carbon focused scan also showed predominantly peaks which correspond to the g-C<sub>3</sub>N<sub>4</sub> photocatalyst support (Figure 3d).

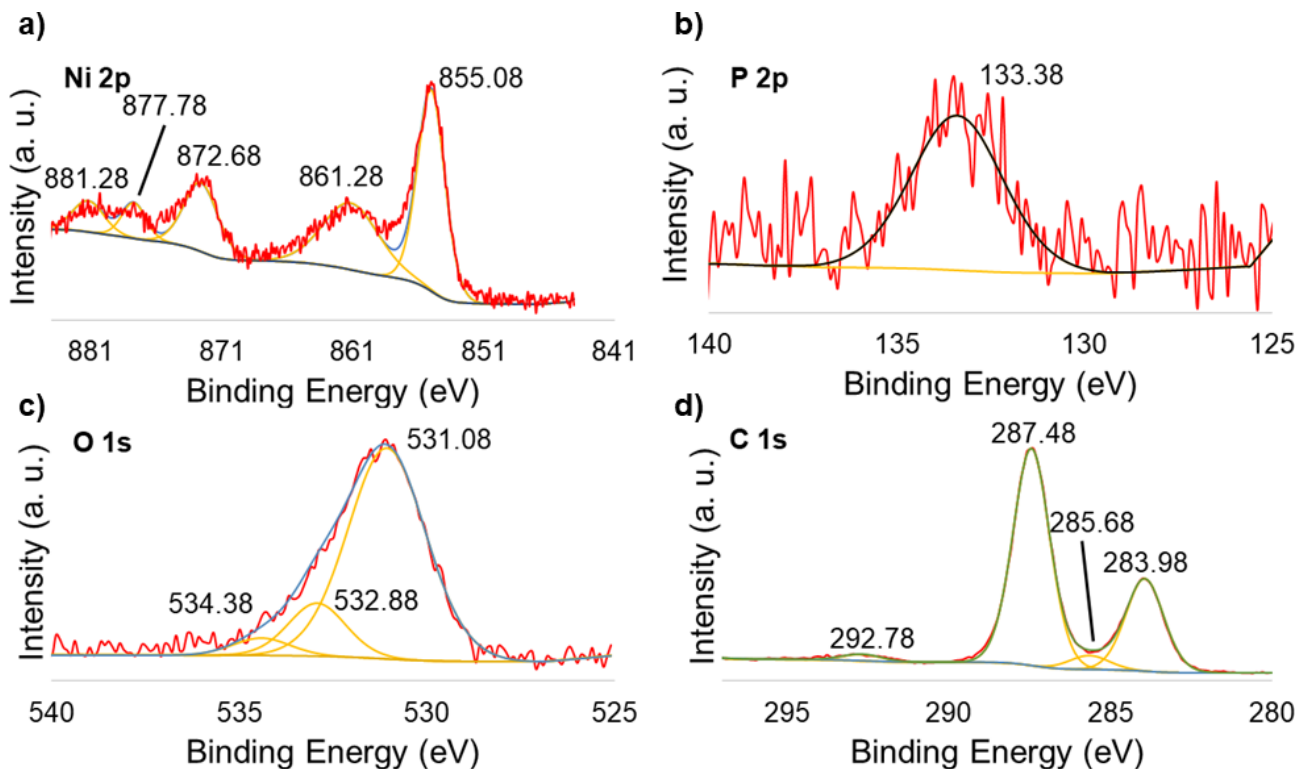


Figure 3. XPS focused scans of a) nickel 2p, b) phosphorus 2p, c) oxygen 1s and d) carbon 1s orbitals of sample CN-NiP-Im-300

The incorporation of the Ni<sub>2</sub>P NP cocatalyst was also evident in ATR-FTIR, although largely overshadowed by the stretches of the g-C<sub>3</sub>N<sub>4</sub> support (Figure S25). The resulting composite showed no significant thermal loss until 500°C under a nitrogen atmosphere (Figure S27) with a final calculated residue after exposure up to 800°C of 2.9%, correlating well with the initial loading of 3 wt% Ni<sub>2</sub>P cocatalyst.

To confirm the proximity of nickel, phosphorus and oxygen in the cocatalyst, elemental mapping of the as-made

and supported nickel phosphide was conducted using high-angle annular dark-field imaging (HAADF). Firstly, the freshly made Ni<sub>2</sub>P NP showed a good intermixing of nickel, phosphorus and oxygen (Figure 4a). This data, paired with XPS data, supports the hypothesis that the nascent cocatalyst consists of a Ni<sub>2</sub>P core, partially coated with a nickel phosphate hydroxide shell, which has been previously shown to occur upon exposure of Ni<sub>2</sub>P to air<sup>61</sup>.

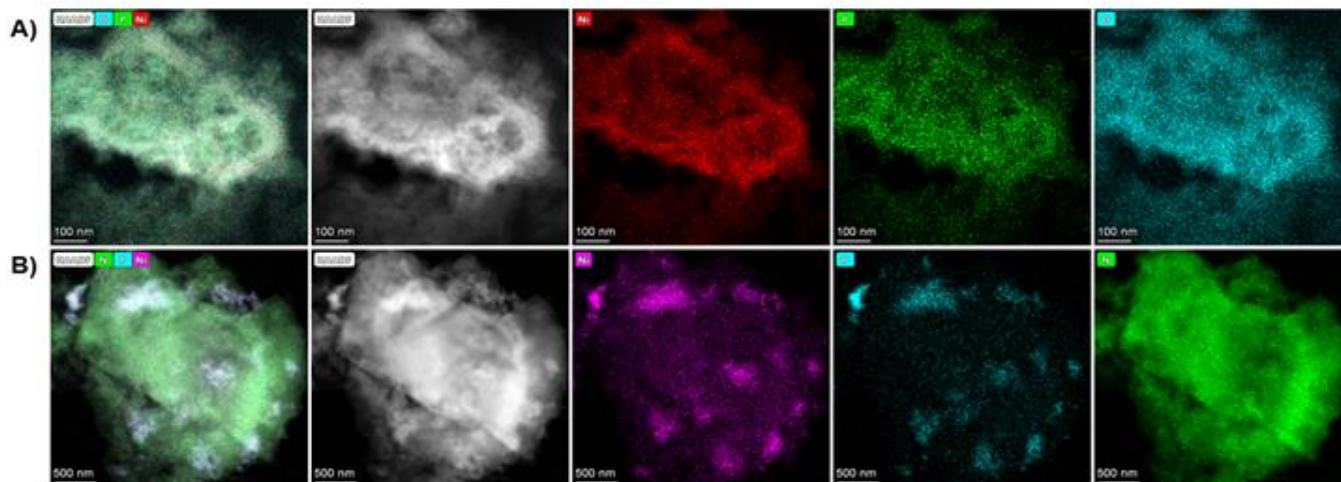


Figure 4. HAADF images of a) as made Ni<sub>2</sub>P (Ni<sub>x</sub>P<sub>y</sub>-5-C17) showing colour mix image over bright field image as well as element focused scans for nickel, phosphorus and oxygen and b) as made CN-NiP-Im-300 showing colour mix image over bright field image as well as element focused scans for nickel, phosphorus and nitrogen

Similar analysis was also conducted on CN-NiP-Im-300 to confirm the thorough incorporation of Ni<sub>2</sub>P NPs within the photoactive g-C<sub>3</sub>N<sub>4</sub> support. Localized domains of Ni<sub>2</sub>P are visible throughout the support (Figure 4b).

#### Photocatalytic water-splitting using Ni<sub>2</sub>P onto g-C<sub>3</sub>N<sub>4</sub>

Next we conducted hydrogen evolution tests by suspending 50 mg of the hybrid nanocatalyst and 5 g of triethanolamine in 100 mL of pure water in an oxygen-free closed reactor. The reactor was irradiated using 100 mW.cm<sup>-2</sup> of simulated sunlight using a broad-spectrum xenon lamp and collecting the evolved hydrogen gas using a gas chromatograph (GC) equipped with a thermal conductivity detector (TCD) to evaluate the hydrogen evolution efficacy of the catalyst (Figure S5). As seen in Figure 6, CN-bulk and CN-NiP-300 exhibited negligible rates of hydrogen evolution. As the temperature of the Ar treatment increased to 400°C (CN-NiP-400), a significant evolution rate of H<sub>2</sub> was obtained, reaching 34.7 μmol g<sup>-1</sup>h<sup>-1</sup>. This result reveals the Ar treatment temperature and, especially, the introduction of Ni<sub>2</sub>P NPs as cocatalyst are essential to activity. A possible mechanism of the photocatalytic H<sub>2</sub> production on Ni<sub>2</sub>P supported g-C<sub>3</sub>N<sub>4</sub> photocatalyst is proposed in Figure 5a. Under the light illumination, electrons and holes separate and accumulate respectively in the conduction band (CB) and the valence band (VB) of g-C<sub>3</sub>N<sub>4</sub>. Electrons transfer to Ni<sub>2</sub>P NP to initiate the H<sub>2</sub>O reduction and form H<sub>2</sub>, while the holes are consumed by TEOA. Due to an electronic structure similar to noble metals (e.g. Pt),<sup>67</sup> Ni<sub>2</sub>P NPs can act as sinks to effectively trap photogenerated electrons from g-C<sub>3</sub>N<sub>4</sub>, leading to enhanced charge separation. Moreover, the distinctive surface allows these NPs to be efficiently active sites for catalytic reduction of H<sub>2</sub>O into H<sub>2</sub>. As previously noted, XPS analysis revealed the nickel phosphide phase with Ni<sup>δ+</sup>-P<sup>δ-</sup> electronic state.<sup>59</sup> This is favorable for the formation of dual-interaction adsorption of H<sub>2</sub>O molecules onto the Ni<sub>2</sub>P NP surface, in which O and H atoms of the H<sub>2</sub>O molecule interact with Ni and P sites, respectively.<sup>68</sup> This dual-interaction adsorption weakens the H-O bonds, thereby facilitating their dissociation during the reduction.<sup>68</sup> The XPS analysis also indicated the formation of PO<sub>4</sub><sup>3-</sup> groups, which can advance the transfer and coupling of protons.<sup>69</sup> Consequently, the photocatalytic H<sub>2</sub> production was significantly promoted in the introduction of partially oxidized Ni<sub>2</sub>P NPs. Interestingly, low temperature of the Ar treatment (300°C) afforded poor results. We hypothesized that the oxygen-free decomposition of heptadecylamine (capping agent used for the initial synthesis) produced at this temperature an amorphous carbon layer with a low degree of graphitization covering the Ni<sub>2</sub>P NP surface.<sup>70</sup> The low graphitization degree of this carbon layer made the electron transfer ineffective, as schematically shown in Figure 5b. When the temperature of treatment in Ar increased to 400°C, the graphitization degree of the carbon layer was slightly improved, allowing few electrons to transfer through this layer to Ni<sub>2</sub>P NPs for the H<sub>2</sub>O reduction. As a result, CN-NiP-400 exhibited a small photoactivity. Thus, both CN-NiP-300 and CN-NiP-400 samples' activity was limited by the presence of heptadecylamine at the Ni<sub>2</sub>P surface which led to hard-to-control carbon layering.

We thus explored ligand exchange prior to g-C<sub>3</sub>N<sub>4</sub> deposition as a means to avoid this problem. With ligand exchanged samples, annealing at 300°C was sufficient to obtain good activity.

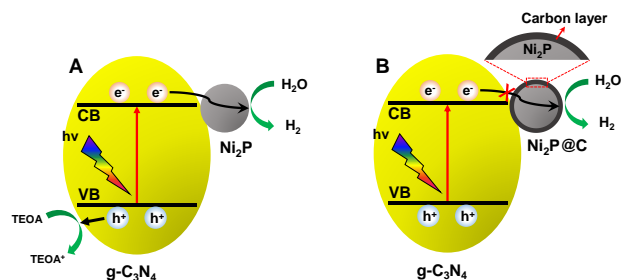


Figure 5. Schematic representation of the electron transfer behaviour between the g-C<sub>3</sub>N<sub>4</sub> support and the Ni<sub>2</sub>P catalyst. Effect of electron transfer a) with and b) without ligand exchange, preventing formation of hindering carbon layer

For the ligand exchanged series of hybrid catalysts (CN-NiP-Im-300 and CN-NiP-Ex-300), heptadecylamine was replaced by TEA cation, making Ni<sub>2</sub>P NPs soluble in water. This facilitates a uniform deposition of Ni<sub>2</sub>P NPs (negative charge) onto the protonated g-C<sub>3</sub>N<sub>4</sub> surface (positive charge). Moreover, TEA cation with low carbon content did not produce a hindering carbon layer during the Ar treatment. Similar ligand exchanges have been shown to improve the hydrogen generation capabilities of both Au<sup>71</sup> and CoP nanocatalysts.<sup>72</sup> Therefore, an intimate interface between g-C<sub>3</sub>N<sub>4</sub> and Ni<sub>2</sub>P NPs was formed that induced an effective electron transfer (Figure 5a). CN-NiP-Ex-300 and CN-NiP-Im-300 showed enhanced H<sub>2</sub> evolution rates of 177.1 μmol g<sup>-1</sup>h<sup>-1</sup> and 233.9 μmol g<sup>-1</sup>h<sup>-1</sup>, respectively, which are much higher than that of samples obtained without prior ligand exchange (CN-NiP series) (Figure 6a). The higher H<sub>2</sub> evolution rate of CN-NiP-Im-300, as compared to CN-NiP-Ex-300, may also be due to the higher amount of deposited Ni<sub>2</sub>P NPs.

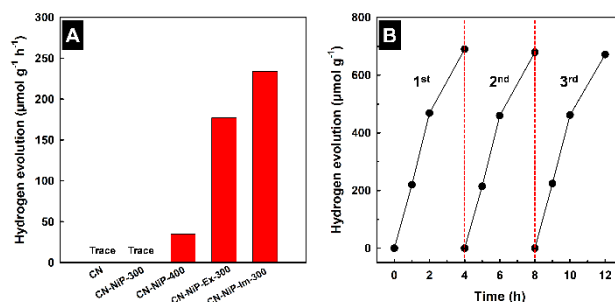


Figure 6. a) H<sub>2</sub> evolution rates of several prepared samples, b) H<sub>2</sub> evolution of CN-NiP-Im-300 for 3 cycles of 4h.

The photocatalytic activity of CN-NiP-Im-300 was tested for three cycles of 4 hours to demonstrate the photostability. As shown in Figure 6b, there was no significant decay in the amount of H<sub>2</sub> evolved after 3 cycles, signifying the photocatalytic stability of CN-NiP-Im-300. To investigate the charge carrier behavior of CN and CN-NiP-Im-300, their transient photocurrent and electrochemical impedance spectroscopy (EIS)

Nyquist plots were measured (Figure 7b). As shown in Figure 7a, the photocurrent of CN-NiP-Im-300 is higher than that of CN, revealing an efficient charge carrier generation and separation<sup>73-76</sup>. Additionally, CN-NiP-Im-300 exhibits a decrease in the impedance, signifying its enhanced charge transferability compared to CN<sup>76-78</sup>. The enhancement of charge carrier separation and transfer of CN-NiP-Im-300 results from the introduction of Ni<sub>2</sub>P NPs, which are the electron sinks and active sites for H<sub>2</sub> evolution, thereby improving the photoactivity.

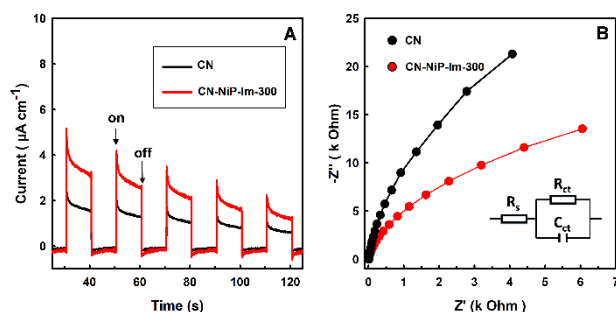


Figure 7. a) Transient photocurrent and b) Electrochemical impedance spectroscopy (EIS) Nyquist plots of CN/FTO and CN-NiP-Im-300/FTO. (Inset Randles circuit used for EIS characterization; R<sub>s</sub> - solution resistance; R<sub>ct</sub> - polarization resistance; C<sub>ct</sub> - double-layer capacitor).

Comparison of our catalyst system to similar systems which use the paired cocatalysts of earth-abundant metal phosphide nanoparticles and g-C<sub>3</sub>N<sub>4</sub>, show competitive hydrogen production values for the Ni<sub>2</sub>P cocatalysts presented herein (Table S2, see ESI for details). While the current state of the art is a paired 0.45 wt% CoP@g-C<sub>3</sub>N<sub>4</sub>, producing up to 1074 μmol g<sup>-1</sup>h<sup>-1</sup> of hydrogen (Table S2, Entry 2), various other earth abundant metal phosphides, such as iron or copper (see Table S2, Entries 3 and 4 in ESI for details) have also been employed with mild success. The effect of the support (Table S2, Entry 5) as well as the specific phase of nickel phosphide tested (Table S2, Entries 6-8) also support the hypothesis of Ni<sub>2</sub>P being the active cocatalyst phase. Interestingly, despite the presence of P-O peaks in the XPS data found in several literature examples, to the best of our knowledge, the influence of the specific amount of surface oxygen in metal phosphides is rarely corroborated systematically to the HER activity. Dreiss and co-workers had investigated the surface changes of nickel phosphide to a mixture of nickel phosphates and hydroxides under alkaline conditions, while still maintaining their efficacy for HER.<sup>79</sup> It is notable that Li and co-workers, and Ye and co-workers both showed that the external addition of K<sub>2</sub>HPO<sub>4</sub> boosted the catalytic activity of both Co<sub>2</sub>P@g-C<sub>3</sub>N<sub>4</sub> (Table S2, Entry 9)<sup>80</sup> and Pt@g-C<sub>3</sub>N<sub>4</sub> respectively.<sup>81</sup> They demonstrated that the H<sub>2</sub>PO<sub>4</sub><sup>-</sup> assisted in both the transport of protons to the active sites of the catalyst as well as increasing the onset potential, implying H<sub>2</sub>PO<sub>4</sub><sup>-</sup> plays an active role in the catalysis.<sup>81</sup> In order to further support the bifunctional nature of the surface of our cocatalyst, we sought to compare to other metal phosphide hydroxide systems. Work

by Neppolian and co-workers demonstrated the use of a cobalt phosphate hydroxide catalyst with hydrogen production values very similar to our work (Table S2, Entry 10).<sup>82</sup> This supports the hypothesis that the surface phosphates seen in our catalysts may also have a bifunctional role, both to provide long term storage stability as well as reactivity of the cocatalyst. The ability to make nickel phosphide nanocatalysts with particle diameter sub 3 nm on a gram scale, all while having comparable hydrogen production values to similar systems which employ nickel phosphide made in solution, show the potential to further expand this mechanochemical methodology to other metal phosphide catalysts. In this proof of concept study, we also measured that our catalyst did not degrade over exposure to air for 2 weeks.

### Comparison of Mass Intensity (MI) and energy usage metrics

In order to support the use of mechanochemistry for the synthesis of TMP nanoparticles, we looked towards the use of both the Mass Intensity (MI) of each synthesis methodology, as well as the energy input required, per gram of product, to demonstrate the viability of mechanochemical methods towards future research in the design of metal phosphide nanomaterials. The Mass Intensity (MI) was calculated as previously reported,<sup>83</sup> shown in Eqn. (1).

$$\text{Mass Intensity} = \text{Total Mass of Process} / \text{Mass of Product} \quad (1)$$

The use of both MI sustainability metrics as well as measuring the energy usage of each method, gave a quantitative comparison of both the small and large scale mechanochemical methods presented in this paper for the bottom-up synthesis of nickel phosphide. While similar metrics have been applied for the synthesis of pure metal nanoparticles or titanium dioxide,<sup>84</sup> to the best of our knowledge, no such analysis has been conducted for a bottom-up mechanochemical synthesis of NPs, however there are examples which show the cost and material benefit of such synthesis for metal-organic framework (MOF) synthesis.<sup>35,85,86</sup> Comparing first our small scale mechanochemical synthesis which produces roughly 100 milligrams to either the milligram synthesis by thermal decomposition of TOP or triphenylphosphite, there is a 2.4- to 18.6-fold decrease of the energy demand per gram of material. At the small scale, there is also a comparable decrease in the mass intensity from 9585 (Table 2, Entry 1) to 3593 (Table 2, Entry 4) for the decomposition of triphenylphosphite by solution methods, while being energetically competitive compared to the decomposition of both triphenylphosphite or TOP (Table 2, Entries 1 and 2). However, these benefits are compounded when scaled up using a planetary mill. Upon scaling up to 2.5 grams in a planetary mill the energy demand drops to 0.03 KWH/g and the MI after washing drops to 101 (Table 2, Entry 5). This MI value is already more than 3 times lower than gram scale synthesis in solution (Table 2, Entry 3) as well as having an 18.7 time decrease in energy demand. These metrics help to further support the sustainability potential of future mechanochemical applications towards nanoparticle synthesis and provide a framework through which other nanoparticle syntheses can be evaluated.

Table 2. Comparison of Mass Indices (MI) and energy demand of other synthetic methodologies to this presented work.

Entry	Method	MI (before washing)	MI (after washing)	Energy Input (KWH/g)
-------	--------	---------------------	--------------------	----------------------

1	Thermal decomposition of tri-phenylphosphite <sup>87a</sup>	1501	9585	29.8
2	Thermal decomposition of TOP <sup>88b</sup>	95.54	1500	3.92
3	Hot injection of triphenylphosphite (1 gram scale) <sup>89c</sup>	76	331	0.562
4	<b>Mechanochemical synthesis with Na<sub>3</sub>P in shaker mill (This work)</b>	1	3593	1.60
5	<b>Mechanochemical synthesis with Na<sub>3</sub>P in planetary mill (This work)</b>	1	101	0.03

<sup>a</sup> These values were the best approximation based on 70% mass yields as well as our energy measurements at similar temperatures

<sup>b</sup> The PIB used showed a max temperature of 290°C, even after 2 hours

<sup>c</sup> These values were the best approximation based on 58% mass yields in ESI as well as our energy measurements at similar temperatures

## Conclusions

We report a simple and rapid synthesis of ultrasmall nickel phosphide nanoparticles suitable for photocatalytic applications, using a mechanochemical methodology that uses sodium phosphide as a readily accessible phosphorus source, while completely avoiding high temperatures and toxic organic solvents. Overall, increasing the length of the chain on the alkyl amine ligand resulted in a decrease in nanoparticle diameter to 2.8 nm, while preventing considerable sintering. The cocatalysts were then paired with a photoactive graphitic carbon nitride support after a simple ligand exchange and showed initial hydrogen production values of 233.9  $\mu\text{mol g}^{-1} \text{h}^{-1}$  after 3 hours using a broad-spectrum Xenon lamp at room temperature, owing to the unique bifunctional surface chemistry of nickel phosphide hydroxide. This preliminary investigation of the viability of mechanochemical activation and aging for the bottom-up synthesis of discrete nanoparticles will be further investigated to better understand the *in-situ* growth kinetics of binary metal phosphides in the solid-state.

## Acknowledgements

We thank the Natural Science and Engineering Research Council of Canada (NSERC) Discovery Grant and accelerator programs, the Canada Foundation for Innovation (CFI), the Canada Research Chairs (CRC), the McGill Sustainability Systems Initiative (MSSI), the Fonds de Recherche du Québec – Nature et Technologies (FRQNT) Equipe program, the Centre for Green Chemistry and Catalysis (CGCC) and McGill University for their financial support. We thank Dr. David Liu and Dr. Boris Nijikovsky of the Facility for Electron Microscopy Research of McGill University for their help in both the imaging and elemental mapping of the nickel phosphide nanoparticles. We thank the MC<sup>2</sup> facility at McGill University for their help in acquiring XRD data.

## Author Contributions

BGF and GD conducted the synthesis and characterization of the Ni<sub>2</sub>P cocatalysts, NNV synthesized the hybrid catalysts as well as conducted all catalytic HER reactions and photochemical analysis. All authors contributed to the writing and editing of this manuscript.

## Supporting Information

Summary of general synthetic and catalytic testing procedures, TEM images, EDX spectroscopy, XPS analysis of nanoparticles

made with trioctylphosphine and planetary scale reaction, stoichiometry analysis, PXRD diffractograms, FTIR spectra, TGA analysis of both free and supported particles and comparison table to previous literature examples.

## REFERENCES

- (1) Michalet, X.; Pinaud, F. F.; Bentolila, J.; Tsay, J. M.; Doose, S.; Li, J. J.; Sundaresan, G.; Wu, A. M.; Gambhir, S. S.; Weiss, S. Quantum Dots for Live Cells, in Vivo Imaging, and Diagnostics. *Science*, **2005**, *307* (5709), 538–544. DOI: 10.1126/science.1104274.
- (2) Hussain, S.; Won, N.; Nam, J.; Bang, J.; Chung, H.; Kim, S. One-Pot Fabrication of High-Quality InP/ZnS (Core/Shell) Quantum Dots and Their Application to Cellular Imaging. *ChemPhysChem*, **2009**, *10* (9–10), 1466–1470. DOI: 10.1002/cphc.200900159.
- (3) Owen, J.; Brus, L. Chemical Synthesis and Luminescence Applications of Colloidal Semiconductor Quantum Dots. *J. Am. Chem. Soc.*, **2017**, *139* (32), 10939–10943. DOI: 10.1021/jacs.7b05267.
- (4) Anantharaj, S.; Ede, S. R.; Sakthikumar, K.; Karthick, K.; Mishra, S.; Kundu, S. Recent Trends and Perspectives in Electrochemical Water Splitting with an Emphasis on Sulfide, Selenide, and Phosphide Catalysts of Fe, Co, and Ni: A Review. *ACS Catal.*, **2016**, *6* (12), 8069–8097. DOI: 10.1021/acscatal.6b02479.
- (5) Chu, S.; Cui, Y.; Liu, N. The Path towards Sustainable Energy. *Nature Mater.*, **2016**, *16* (1), 16–22. DOI: 10.1038/nmat4834.
- (6) Cova, C. M.; Zuliani, A.; Puente Santiago, A. R.; Caballero, A.; Muñoz-Batista, M. J.; Luque, R. Microwave-Assisted Preparation of Ag/Ag<sub>2</sub>S Carbon Hybrid Structures from Pig Bristles as Efficient HER Catalysts. *J. Mater. Chem. A*, **2018**, *6* (43), 21516–21523. DOI: 10.1039/C8TA06417B.
- (7) Shi, Y.; Zhang, B. Recent Advances in Transition Metal Phosphide Nanomaterials: Synthesis and Applications in Hydrogen Evolution Reaction. *Chem. Soc. Rev.*, **2016**, *45* (6), 1529–1541. DOI: 10.1039/C5CS00434A.
- (8) Callejas, J. F.; Read, C. G.; Roske, C. W.; Lewis, N. S.; Schaak, R. E. Synthesis, Characterization, and Properties of Metal Phosphide Catalysts for the Hydrogen-Evolution Reaction. *Chem. Mater.* **2016**, *28* (17), 6017–6044.
- (9) Feng, L.; Xue, H. Advances in Transition-Metal Phosphide Applications in Electrochemical Energy Storage and Catalysis. *ChemElectroChem.*, **2017**, *4* (1), 20–34. DOI: 10.1002/celec.201600563.
- (10) Feng, L.; Vrabel, H.; Bensimon, M.; Hu, X. Easily-Prepared Dinickel Phosphide (Ni<sub>2</sub>P) Nanoparticles as an Efficient and Robust Electrocatalyst for Hydrogen Evolution. *Phys. Chem. Chem. Phys.*, **2014**, *16* (13), 5917. DOI: 10.1039/C4CP00482E.

- (11) Clark, P.; Li, W.; Oyama, S. T. Synthesis and Activity of a New Catalyst for Hydroprocessing: Tungsten Phosphide. *J. Catal.* **2001**, *200* (1), 140–147. DOI: 10.1006/jcat.2001.3189.
- (12) Oyama, S. T. Novel Catalysts for Advanced Hydroprocessing: Transition Metal Phosphides. *J. Catal.*, **2003**, *216* (1–2), 343–352. DOI: 10.1016/S0021-9517(02)00069-6.
- (13) Senevirathne, K.; Burns, A. W.; Bussell, M. E.; Brock, S. L. Synthesis and Characterization of Discrete Nickel Phosphide Nanoparticles: Effect of Surface Ligation Chemistry on Catalytic Hydrodesulfurization of Thiophene. *Adv. Funct. Mater.*, **2007**, *17* (18), 3933–3939. DOI: 10.1002/adfm.200700758.
- (14) Stinner, C.; Prins, R.; Weber, T. Formation, Structure, and HDN Activity of Unsupported Molybdenum Phosphide. *J. Catal.*, **2000**, *191* (2), 438–444. DOI: 10.1006/jcat.1999.2808.
- (15) Stinner, C.; Prins, R.; Weber, T. Binary and Ternary Transition-Metal Phosphides as HDN Catalysts. *J. Catal.* **2001**, *202* (1), 187–194. DOI: 10.1006/jcat.2001.3283.
- (16) Yu, Z.; Wang, Y.; Sun, Z.; Li, X.; Wang, A.; Camaioni, D. M.; Lercher, J. A. Ni<sub>3</sub>P as a High-Performance Catalytic Phase for the Hydrodeoxygenation of Phenolic Compounds. *Green Chem.*, **2018**, *20* (3), 609–619. DOI: 10.1039/C7GC03262E.
- (17) Bui, P.; Cecilia, J. A.; Oyama, S. T.; Takagaki, A.; Infantes-Molina, A.; Zhao, H.; Li, D.; Rodríguez-Castellón, E.; Jiménez López, A. Studies of the Synthesis of Transition Metal Phosphides and Their Activity in the Hydrodeoxygenation of a Biofuel Model Compound. *J. Catal.*, **2012**, *294*, 184–198. DOI: 10.1016/j.jcat.2012.07.021.
- (18) Wu, S. K.; Lai, P. C.; Lin, Y. C.; Wan, H. P.; Lee, H. T.; Chang, Y. H. Atmospheric Hydrodeoxygenation of Guaiacol over Alumina-, Zirconia-, and Silica-Supported Nickel Phosphide Catalysts. *ACS Sustainable Chem. Eng.*, **2013**, *1* (3), 349–358. DOI: 10.1021/sc300157d.
- (19) Li, K.; Wang, R.; Chen, J. Hydrodeoxygenation of Anisole over Silica-Supported Ni<sub>2</sub>P, MoP, and NiMoP Catalysts. *Energy Fuels*, **2011**, *25* (3), 854–863. DOI: 10.1021/ef101258j.
- (20) Chakraborty, I. N.; Roy, S.; Devatha, G.; Rao, A.; Pillai, P. P. InP/ZnS Quantum Dots as Efficient Visible-Light Photocatalysts for Redox and Carbon–Carbon Coupling Reactions. *Chem. Mater.*, **2019**, *31* (7), 2258–2262. DOI: 10.1021/acs.chemmater.9b00086.
- (21) Bang, E.; Choi, Y.; Cho, J.; Suh, Y. H.; Ban, H. W.; Son, J. S.; Park, J. Large-Scale Synthesis of Highly Luminescent InP@ZnS Quantum Dots Using Elemental Phosphorus Precursor. *Chem. Mater.*, **2017**, *29* (10), 4236–4243. DOI: 10.1021/acs.chemmater.7b00254.
- (22) Carenco, S.; Resa, I.; Le Goff, X.; Le Floch, P.; Mézailles, N. White Phosphorus as Single Source of “P” in the Synthesis of Nickel Phosphide. *Chem. Commun.*, **2008**, *22*, 2568–2570. DOI: 10.1039/B802454E.
- (23) Carenco, S.; Le Goff, X. F.; Shi, J.; Roiban, L.; Ersen, O.; Boissière, C.; Sanchez, C.; Mézailles, N. Magnetic Core-Shell Nanoparticles from Nanoscale-Induced Phase Segregation. *Chem. Mater.*, **2011**, *23* (8), 2270–2277. DOI: 10.1021/cm200575g.
- (24) Henkes, A. E.; Vasquez, Y.; Schaak, R. E. Converting Metals into Phosphides: A General Strategy for the Synthesis of Metal Phosphide Nanocrystals. *J. Am. Chem. Soc.*, **2007**, *129* (7), 1896–1897. DOI: 10.1021/ja068502l.
- (25) Liu, J.; Chen, X.; Shao, M.; An, C.; Yu, W.; Qian, Y. Surfactant-Aided Solvothermal Synthesis of Dinickel Phosphide Nanocrystallites Using Red Phosphorus as Starting Materials. *J. Cryst. Growth.*, **2003**, *252* (1–3), 297–301. DOI: 10.1016/S0022-0248(03)00939-4.
- (26) Kovnir, K. A.; Kolen'ko, Y. V.; Ray, S.; Li, J.; Watanabe, T.; Itoh, M.; Yoshimura, M.; Shevelkov, A. V. A Facile High-Yield Solvothermal Route to Tin Phosphide Sn<sub>4</sub>P<sub>3</sub>. *J. Solid State Chem.*, **2006**, *179* (12), 3756–3762. DOI: 10.1016/j.jssc.2006.08.012.
- (27) Friščić, T.; Mottillo, C.; Titl, H. M. Mechanochemistry for Synthesis. *Angew. Chem. Int. Ed.*, **2020**, *59* (3), 1018–1029. DOI: 10.1002/anie.201906755.
- (28) Ravnsbæk, J. B.; Swager, T. M. Mechanochemical Synthesis of Poly(Phenylene Vinylenes). *ACS Macro Lett.* **2014**, *3* (4), 305–309. DOI: 10.1021/mz500098r.
- (29) Huang, J.; Moore, J. A.; Acquaye, J. H.; Kaner, R. B. Mechanochemical Route to the Conducting Polymer Polyaniline. *Macromolecules* **2005**, *38* (2), 317–321. DOI: 10.1021/ma049711y.
- (30) Ashlin, M.; Hobbs, C. E. Post-Polymerization Thiol Substitutions Facilitated by Mechanochemistry. *Macromol. Chem. Phys.* **2019**, *220* (21), 1900350. DOI: 10.1002/macp.201900350.
- (31) Fiss, B. G.; Hatherly, L.; Stein, R. S.; Friščić, T.; Moores, A. Mechanochemical Phosphorylation of Polymers and Synthesis of Flame-Retardant Cellulose Nanocrystals. *ACS Sustainable Chem. Eng.* **2019**, *7* (8), 7951–7959. DOI: 10.1021/acssuschemeng.9b00764.
- (32) Jodowski, A. D.; Yépez, A.; Luque, R.; Camacho, L.; de Miguel, G. Benign-by-Design Solventless Mechanochemical Synthesis of Three-, Two-, and One-Dimensional Hybrid Perovskites. *Angew. Chem. Int. Ed.* **2016**, *55* (48), 14972–14977. DOI: 10.1002/anie.201607397.
- (33) Klimakow, M.; Klobes, P.; Thünemann, A. F.; Rademann, K.; Emmerling, F. Mechanochemical Synthesis of Metal-Organic Frameworks: A Fast and Facile Approach toward Quantitative Yields and High Specific Surface Areas. *Chem. Mater.* **2010**, *22* (18), 5216–5221. DOI: 10.1021/cm1012119.
- (34) Lv, D.; Chen, Y.; Li, Y.; Shi, R.; Wu, H.; Sun, X.; Xiao, J.; Xi, H.; Xia, Q.; Li, Z. Efficient Mechanochemical Synthesis of MOF-5 for Linear Alkanes Adsorption. *J. Chem. Eng. Data* **2017**, *62* (7), 2030–2036. DOI: 10.1021/acs.jced.7b00049.
- (35) Julien, P. A.; Mottillo, C.; Friščić, T. Metal–Organic Frameworks Meet Scalable and Sustainable Synthesis. *Green Chem.* **2017**, *19* (12), 2729–2747. DOI: 10.1039/C7GC01078H.
- (36) Gomollón-Bel, F. Ten Chemical Innovations That Will Change Our World: IUPAC identifies emerging technologies in Chemistry with potential to make our planet more sustainable. *Chem. Int.* **2019**, *41* (2), 12–17. DOI: 10.1515/ci-2019-0203.
- (37) Gečiąuskaitė, A. A.; García, F. Main Group Mechanochemistry. *Beilstein J. Org. Chem.*, **2017**, *13*, 2068–2077. DOI: 10.3762/bjoc.13.204.
- (38) Sim, Y.; Shi, Y. X.; Ganguly, R.; Li, Y.; García, F. Mechanochemical Synthesis of Phosphazane-Based Frameworks. *Chem. Eur. J.*, **2017**, *23* (47), 11279–11285. DOI: 10.1002/chem.201701619.
- (39) Shi, Y. X.; Xu, K.; Clegg, J. K.; Ganguly, R.; Hirao, H.; Friščić, T.; García, F. The First Synthesis of the Sterically Encumbered Adamantoid Phosphazane P<sub>4</sub>(N<sup>t</sup>Bu)<sub>6</sub>: Enabled by Mechanochemistry. *Angew. Chem. Int. Ed.*, **2016**, *55* (41), 12736–12740. DOI: 10.1002/anie.201605936.
- (40) Li, L.; Protière, M.; Reiss, P. Economic Synthesis of High Quality InP Nanocrystals Using Calcium Phosphide as the Phosphorus Precursor. *Chem. Mater.*, **2008**, *20* (8), 2621–2623. DOI: 10.1021/cm7035579.
- (41) Parkin, I. P. Solid State Metathesis Reaction for Metal Borides, Silicides, Pnictides and Chalcogenides: Ionic or Elemental Pathways. *Chem. Soc. Rev.*, **1996**, *25* (3), 199–207. DOI: 10.1039/CS9962500199.
- (42) Hayashi, A.; Inoue, A.; Tatsumisago, M. Electrochemical Performance of NiP<sub>2</sub> Negative Electrodes in All-Solid-State Lithium Secondary Batteries. *J. Power Sources*, **2009**, *189* (1), 669–671. DOI: 10.1016/j.jpowsour.2008.09.047.
- (43) Pöhls, J. H.; Faghaninia, A.; Petretto, G.; Aydemir, U.; Ricci, F.; Li, G.; Wood, M.; Ohno, S.; Hautier, G.; Snyder, G. J.; et al. Metal Phosphides as Potential Thermoelectric Materials. *J. Mater. Chem. C.*, **2017**, *5* (47), 12441–12456. DOI: 10.1039/C7TC03948D.
- (44) Takacs, L.; Mandal, S. K. Preparation of Some Metal Phosphides by Ball Milling. *Mater. Sci. Eng. A*, **2001**, *304–306* (1–2), 429–433. DOI: 10.1016/S0921-5093(00)01487-8.
- (45) Cossairt, B. M. Shining Light on Indium Phosphide Quantum Dots: Understanding the Interplay among Precursor Conversion, Nucleation, and Growth. *Chem. Mater.* **2016**, *28* (20), 7181–7189. DOI: 10.1021/acs.chemmater.6b03408.
- (46) Rodríguez-Padrón, D.; Puente-Santiago, A. R.; Balu, A. M.;

- Muñoz-Batista, M. J.; Luque, R. Environmental Catalysis: Present and Future. *ChemCatChem*, **2019**, *11* (1), 18–38. DOI: 10.1002/cctc.201801248.
- (47) Xu, C.; Nasrollahzadeh, M.; Sajjadi, M.; Maham, M.; Luque, R.; Puente-Santiago, A. R. Benign-by-Design Nature-Inspired Nanosystems in Biofuels Production and Catalytic Applications. *Renew. Sust. Energ. Rev.*, **2019**, *112*, 195–252. DOI: 10.1016/j.rser.2019.03.062.
- (48) Rak, M. J.; Saadé, N. K.; Friščić, T.; Moores, A. Mechanochemical Synthesis of Ultra-Small Monodisperse Amine-Stabilized Gold Nanoparticles with Controllable Size. *Green Chem.*, **2014**, *16* (1), 86–89. DOI: 10.1039/C3GC41827H.
- (49) Malca, M. Y.; Bao, H.; Bastaille, T.; Saadé, N. K.; Kinsella, J. M.; Friščić, T.; Moores, A. Mechanically Activated Solvent-Free Assembly of Ultrasmall Bi<sub>2</sub>S<sub>3</sub> Nanoparticles: A Novel, Simple, and Sustainable Means to Access Chalcogenide Nanoparticles. *Chem. Mater.*, **2017**, *29* (18), 7766–7773. DOI: 10.1021/acs.chemmater.7b02134.
- (50) Baláž, P.; Havlík, T.; Bastl, Z.; Briančin, J. Mechanochemical Synthesis of Iron Sulphides. *J. Mater. Sci. Lett.*, **1995**, *14*, 344–346. DOI: 10.1007/BF00592145.
- (51) Baláž, P.; Baláž, M.; Achimovičová, M.; Bujňáková, Z.; Dutková, E. Chalcogenide Mechanochemistry in Materials Science: Insight into Synthesis and Applications (a Review). *J. Mater. Sci.*, **2017**, *52* (20), 11851–11890. DOI: 10.1007/s10853-017-1174-7.
- (52) Baláž, P.; Bálintová, M.; Bastl, Z.; Briančin, J.; Šepelák, V. Characterization and Reactivity of Zinc Sulphide Prepared by Mechanochemical Synthesis. *Solid State Ionics*, **1997**, *101*, 45–51. DOI: 10.1016/S0167-2738(97)84007-6.
- (53) Achimovičová, M.; Daneu, N.; Rečnik, A.; Ďurišin, J.; Baláž, P.; Fabián, M.; Kováč, J.; Šatka, A. Characterization of Mechanochemically Synthesized Lead Selenide. *Chem. Pap.*, **2009**, *63* (5), 562–567. DOI: 10.2478/s11696-009-0050-6.
- (54) Shalabayev, Z.; Baláž, M.; Daneu, N.; Dutková, E.; Bujňáková, Z.; Kaňuchová, M.; Danková, Z.; Balážová, L.; Urakaev, F.; Tkáčiková, L.; et al. Sulfur-Mediated Mechanochemical Synthesis of Spherical and Needle-Like Copper Sulfide Nanocrystals with Antibacterial Activity. *ACS Sustainable Chem. Eng.*, **2019**, *7* (15), 12897–12909. DOI: 10.1021/acssuschemeng.9b01849.
- (55) Baláž, P.; Hegedüs, M.; Achimovičová, M.; Baláž, M.; Tešínský, M.; Dutková, E.; Kaňuchová, M.; Briančin, J. Semi-Industrial Green Mechanochemical Syntheses of Solar Cell Absorbers Based on Quaternary Sulfides. *ACS Sustainable Chem. Eng.*, **2018**, *6* (2), 2132–2141. DOI: 10.1021/acssuschemeng.7b03563.
- (56) Rodríguez-Padrón, D.; Puente-Santiago, A. R.; Luna-Lama, F.; Caballero, A.; Muñoz-Batista, M. J.; Luque, R. Versatile Protein-Templated TiO<sub>2</sub> Nanocomposite for Energy Storage and Catalytic Applications. *ACS Sustainable Chem. Eng.*, **2019**, *7* (5), 5329–5337. DOI: 10.1021/acssuschemeng.8b06349.
- (57) Rodríguez-Padrón, D.; Puente-Santiago, A. R.; Cano, M.; Caballero, A.; Muñoz-Batista, M. J.; Luque, R. Improving Electrochemical Hydrogen Evolution of Ag@CN Nanocomposites by Synergistic Effects with α-Rich Proteins. *ACS Appl. Mater. Interfaces*, **2020**, *12* (2), 2207–2215. DOI: 10.1021/acsmi.9b13571.
- (58) Muñoz-Batista, M. J.; Rodríguez-Padrón, D.; Puente-Santiago, A. R.; Luque, R. Mechanochemistry: Toward Sustainable Design of Advanced Nanomaterials for Electrochemical Energy Storage and Catalytic Applications. *ACS Sustainable Chem. Eng.*, **2018**, *6* (8), 9530–9544. DOI: 10.1021/acssuschemeng.8b01716.
- (59) Jiang, P.; Liu, Q.; Ge, C.; Cui, W.; Pu, Z.; Asiri, A. M.; Sun, X. CoP Nanostructures with Different Morphologies: Synthesis, Characterization and a Study of Their Electrochemical Performance toward the Hydrogen Evolution Reaction. *J. Mater. Chem. A*, **2014**, *2* (35), 14634–14640. DOI: 10.1039/C4TA03261F.
- (60) Tang, C.; Zhang, R.; Lu, W.; Wang, Z.; Liu, D.; Hao, S.; Du, G.; Asiri, A. M.; Sun, X. Energy-Saving Electrolytic Hydrogen Generation: Ni<sub>2</sub>P Nanoarray as a High-Performance Non-Noble-Metal Electrocatalyst. *Angew. Chem. Int. Ed.*, **2017**, *56* (3), 842–846. DOI: 10.1002/anie.201608899.
- (61) Huang, Z.; Chen, Z.; Chen, Z.; Lv, C.; Meng, H.; Zhang, C. Ni<sub>12</sub>P<sub>5</sub> Nanoparticles as an Efficient Catalyst for Hydrogen Generation via Electrolysis and Photoelectrolysis. *ACS Nano*, **2014**, *8* (8), 8121–8129. DOI: 10.1021/nn5022204.
- (62) Yuan, C. Z.; Jiang, Y. F.; Wang, Z.; Xie, X.; Yang, Z. K.; Yousaf, A. Bin; Xu, A. W. Cobalt Phosphate Nanoparticles Decorated with Nitrogen-Doped Carbon Layers as Highly Active and Stable Electrocatalysts for the Oxygen Evolution Reaction. *J. Mater. Chem. A*, **2016**, *4* (21), 8155–8160. DOI: 10.1039/C6TA01929C.
- (63) Wang, Y.; Asunskis, D. J.; Sherwood, P. M. A. Iron (II) Phosphate (Fe<sub>3</sub>(PO<sub>4</sub>)<sub>2</sub>) by XPS. *Surf. Sci. Spectra* **2002**, *9* (1), 91–98. DOI: 10.1116/11.20030105.
- (64) Al-Omair, M. A.; Touny, A. H.; Saleh, M. M. Reflux-Based Synthesis and Electrocatalytic Characteristics of Nickel Phosphate Nanoparticles. *J. Power Sources* **2017**, *342*, 1032–1039. DOI: 10.1016/j.jpowsour.2016.09.079.
- (65) Cao, S.; Chen, Y.; Wang, C. J.; He, P.; Fu, W. F. Highly Efficient Photocatalytic Hydrogen Evolution by Nickel Phosphide Nanoparticles from Aqueous Solution. *Chem. Commun.*, **2014**, *50* (72), 10427–10429. DOI: 10.1039/C4CC05026F.
- (66) Jung, C. S.; Park, K.; Lee, Y.; Kwak, I. H.; Kwon, I. S.; Kim, J.; Seo, J.; Ahn, J. P.; Park, J. Nickel Phosphide Polymorphs with an Active (001) Surface as Excellent Catalysts for Water Splitting. *CrystEngComm*, **2019**, *21* (7), 1143–1149. DOI: 10.1039/C8CE01884G.
- (67) Cao, S.; Wang, C.-J.; Fu, W.-F.; Chen, Y. Metal Phosphides as Co-Catalysts for Photocatalytic and Photoelectrocatalytic Water Splitting. *ChemSusChem*, **2017**, *10* (22), 4306–4323. DOI: 10.1002/cssc.201701450.
- (68) Zhang, R.; Wang, X.; Yu, S.; Wen, T.; Zhu, X.; Yang, F.; Sun, X.; Wang, X.; Hu, W. Ternary NiCo<sub>2</sub>P<sub>x</sub> Nanowires as pH-Universal Electrocatalysts for Highly Efficient Hydrogen Evolution Reaction. *Adv. Mater.*, **2017**, *29* (9), 1605502. DOI: 10.1002/adma.201605502.
- (69) Zhao, J.; Tran, P. D.; Chen, Y.; Loo, J. S. C.; Barber, J.; Xu, Z. J. Achieving High Electrocatalytic Efficiency on Copper: A Low-Cost Alternative to Platinum for Hydrogen Generation in Water. *ACS Catal.*, **2015**, *5* (7), 4115–4120. DOI: 10.1021/acscatal.5b00556.
- (70) Barbera, K.; Frusteri, L.; Italiano, G.; Spadaro, L.; Frusteri, F.; Perathoner, S.; Centi, G. Low-Temperature Graphitization of Amorphous Carbon Nanospheres. *Chinese J. Catal.*, **2014**, *35* (6), 869–876. DOI: 10.1016/S1872-2067(14)60098-X.
- (71) Alba-Molina, D.; Puente Santiago, A. R.; Giner-Casares, J. J.; Rodríguez-Castellón, E.; Martín-Romero, M. T.; Camacho, L.; Luque, R.; Cano, M. Tailoring the ORR and HER Electrocatalytic Performances of Gold Nanoparticles through Metal-Ligand Interfaces. *J. Mater. Chem. A*, **2019**, *7* (35), 20425–20434. DOI: 10.1039/C9TA05492H.
- (72) Delley, M. F.; Wu, Z.; Mundy, M. E.; Ung, D.; Cossairt, B. M.; Wang, H.; Mayer, J. M. Hydrogen on Cobalt Phosphide. *J. Am. Chem. Soc.*, **2019**, *141* (38), 15390–15402. DOI: 10.1021/jacs.9b07986.
- (73) Vu, N. N.; Kaliaguine, S.; Do, T. O. Selective Fragmentation through C–N Bond Cleavage of Carbon Nitride Framework for Enhanced Photocatalytic Hydrogen Production. *ACS Sustainable Chem. Eng.*, **2020**, *8* (2), 853–863. DOI: 10.1021/acssuschemeng.9b05083.
- (74) Vu, N. N.; Nguyen, C. C.; Kaliaguine, S.; Do, T. O. Synthesis of g-C<sub>3</sub>N<sub>4</sub> Nanosheets by Using a Highly Condensed Lamellar Crystalline Melamine–Cyanuric Acid Supramolecular Complex for Enhanced Solar Hydrogen Generation. *ChemSusChem*, **2019**, *12* (1), 291–302. DOI: 10.1002/cssc.201802394.
- (75) Vu, M. H.; Sakar, M.; Nguyen, C. C.; Do, T. O. Chemically Bonded Ni Cocatalyst onto the S Doped g-C<sub>3</sub>N<sub>4</sub> Nanosheets and Their

- Synergistic Enhancement in H<sub>2</sub> Production under Sunlight Irradiation. *ACS Sustainable Chem. Eng.*, **2018**, 6 (3), 4194–4203. DOI: 10.1021/acssuschemeng.7b04598
- (76) Han, X.; Tian, L.; Jiang, H.; Kong, L.; Lv, J.; Shan, J.; Wang, J.; Fan, X. Facile Transformation of Low Cost Melamine-Oxalic Acid into Porous Graphitic Carbon Nitride Nanosheets with High Visible-Light Photocatalytic Performance. *RSC Adv.*, **2017**, 7 (24), 14372–14381. DOI: 10.1039/c7ra01205e.
- (77) Liu, J.; Liu, Y.; Liu, N.; Han, Y.; Zhang, X.; Huang, H.; Lifshitz, Y.; Lee, S. T.; Zhong, J.; Kang, Z. Metal-Free Efficient Photocatalyst for Stable Visible Water Splitting via a Two-Electron Pathway. *Science*, **2015**, 347 (6225), 970–974. DOI: 10.1126/science.aaa3145.
- (78) Wang, Y.; Hong, J.; Zhang, W.; Xu, R. Carbon Nitride Nanosheets for Photocatalytic Hydrogen Evolution: Remarkably Enhanced Activity by Dye Sensitization. *Catal. Sci. Technol.*, **2013**, 3 (7), 1703–1711. DOI: 10.1039/C3CY20836B.
- (79) Menezes, P. W.; Indra, A.; Das, C.; Walter, C.; Göbel, C.; Gutkin, V.; Schmeißer, D.; Driess, M. Uncovering the Nature of Active Species of Nickel Phosphide Catalysts in High-Performance Electrochemical Overall Water Splitting. *ACS Catal.*, **2017**, 7 (1), 103–109. DOI: 10.1021/acscatal.6b02666.
- (80) Shen, R.; Xie, J.; Zhang, H.; Zhang, A.; Chen, X.; Li, X. Enhanced Solar Fuel H<sub>2</sub> Generation over g-C<sub>3</sub>N<sub>4</sub> Nanosheet Photocatalysts by the Synergetic Effect of Noble Metal-Free Co<sub>2</sub>P Cocatalyst and the Environmental Phosphorylation Strategy. *ACS Sustainable Chem. Eng.* **2018**, 6 (1), 816–826. DOI: 10.1021/acssuschemeng.7b03169.
- (81) Liu, G.; Wang, T.; Zhang, H.; Meng, X.; Hao, D.; Chang, K.; Li, P.; Kako, T.; Ye, J. Nature-Inspired Environmental “Phosphorylation” Boosts Photocatalytic H<sub>2</sub> Production over Carbon Nitride Nanosheets under Visible-Light Irradiation. *Angew. Chem. Int. Ed.* **2015**, 54 (46), 13561–13565. DOI: 10.1002/anie.201505802.
- (82) Lakhera, S. K.; Vijayarajan, V. S.; Rishi Krishna, B. S.; Veluswamy, P.; Neppolian, B. Cobalt Phosphate Hydroxide Loaded g-C<sub>3</sub>N<sub>4</sub> Photocatalysts and Its Hydrogen Production Activity. *Int. J. Hydrogen Energy* **2020**, 45 (13), 7562–7573. DOI: 10.1016/j.ijhydene.2019.07.202.
- (83) Sheldon, R. A. Metrics of Green Chemistry and Sustainability: Past, Present, and Future. *ACS Sustainable Chem. Eng.* **2018**, 6 (1), 32–48. DOI: 10.1021/acssuschemeng.7b03505.
- (84) Albrecht, M. A.; Evans, C. W.; Raston, C. L. Green Chemistry and the Health Implications of Nanoparticles. *Green Chem.* **2006**, 8 (5), 417–432. DOI: 10.1039/B517131H.
- (85) Cliffe, M. J.; Mottillo, C.; Stein, R. S.; Bučar, D. K.; Friščić, T. Accelerated Aging: A Low Energy, Solvent-Free Alternative to Solvothermal and Mechanochemical Synthesis of Metal-Organic Materials. *Chem. Sci.* **2012**, 3 (8), 2495–2500. DOI: 10.1039/C2SC20344H.
- (86) DeSantis, D.; Mason, J. A.; James, B. D.; Houchins, C.; Long, J. R.; Veenstra, M. Techno-Economic Analysis of Metal-Organic Frameworks for Hydrogen and Natural Gas Storage. *Energy Fuels* **2017**, 31 (2), 2024–2032. DOI: 10.1021/acs.energyfuels.6b02510.
- (87) Liu, J.; Meyns, M.; Zhang, T.; Arbiol, J.; Cabot, A.; Shavel, A. Triphenyl Phosphite as the Phosphorus Source for the Scalable and Cost-Effective Production of Transition Metal Phosphides. *Chem. Mater.* **2018**, 30 (5), 1799–1807. DOI: 10.1021/acs.chemmater.8b00290.
- (88) Popczun, E. J.; McKone, J. R.; Read, C. G.; Biacchi, A. J.; Wiltrout, A. M.; Lewis, N. S.; Schaak, R. E. Nanostructured Nickel Phosphide as an Electrocatalyst for the Hydrogen Evolution Reaction. *J. Am. Chem. Soc.* **2013**, 135 (25), 9267–9270. DOI: 10.1021/ja403440e.
- (89) Andaraarachchi, H. P.; Thompson, M. J.; White, M. A.; Fan, H. J.; Vela, J. Phase-Programmed Nanofabrication: Effect of Organophosphite Precursor Reactivity on the Evolution of Nickel and Nickel Phosphide Nanocrystals. *Chem. Mater.* **2015**, 27 (23), 8021–8031. DOI: 10.1021/acs.chemmater.5b03506.



For Table of Contents Use Only

Synopsis: This paper presents the solvent-free mechanochemical synthesis of nickel phosphide nanocatalysts for the hydrogen evolution reaction under mild conditions.